Cislunar Orbit Determination Behavior: Processing Observations of Periodic Orbits with Gaussian Mixture Model Estimation Filters

C. Channing Chow II[1], Charles J. Wetterer[2], Jason, Baldwin[3], Micah Dilley[2], Keric Hill[2], Paul Billings[2], and James Frith[4]
[1]Cloudstone Innovations, [2]KBR, [3]Complex Futures,
[4]Air Force Research Laboratory

ABSTRACT

Orbits of objects in cislunar space are, in general, non-Keplerian due to the influence of the Moon's gravity and cannot be generically parameterized by a simple set of characteristics. Objects are also fainter and move relatively more slowly when viewed from Earth. Detection and tracking are expected to be significantly more difficult and, as a consequence, orbit determination becomes more challenging. In this paper we review a subset of possible orbits and their expected astrometric and photometric signatures from the perspective of hypothetical ground-based electro-optical sensors on Earth. Although a multitude of orbits are possible, we focus on special types of orbits that are closed in the synodic frame (i.e., periodic) and emanate from the libration points of the Earth-Moon system. We investigate three separate elemental periodic orbit families that have been differentially corrected in a high-fidelity dynamical system: H1, L1, and W4W5. For each family, we set objects at different locations at different epochs and simulate the expected observational features (e.g., right ascension, declination, visual magnitude) based on faceted satellite models. In this study, we show how Gaussian mixture model estimation filters behave when processing different observation sets, specifically varying data cadence, data density, data quality, and data span. Convergence and uncertainty bounds are shown to have a strong dependence on the observational data composition (affecting the accuracy of fitting orbits) and a notable correlation to orbital stability (affecting the ability to predict/correct orbits).

1. INTRODUCTION

Our previous paper [1] provided an overview of the expected photometric and astrometric measurements of objects in cislunar orbits, specifically the families of elemental periodic orbits [2] obtained by employing the Circular Restricted 3-Body Problem (CR3BP). As noted, there are some challenges associated with cislunar orbits, particularly in tracking and orbit determination since the objects are both fainter (longer distances will stress remote sensing capabilities) and slower (longer time scales means more observations necessary to see significant fractions of orbits). Additionally, cislunar orbits are very sensitive to initial conditions where orbits are only marginally stable to unstable [3]; small perturbations can lead to wildly disproportionate outcomes (e.g., when approaching a chaos boundary).

In this paper we explore these difficulties in tracking cislunar objects in more detail. Specifically, we investigate three distinct but related elemental periodic orbit families that cover a large portion of cislunar space: H1[1], L1, and W4W5. Select members from these orbital families are differentially corrected from the CR3BP into a high-fidelity dynamical system to find the full-ephemeris analogs of the idealized orbits afforded by the toy problem. With our state space defined, we obtain our measurement space by simulating observational data from three notional Earth ground-based electro-optical systems. The details of the orbits, the measurement generation methodology, and decimation strategy are described in the next section. For the estimation engine, we employ a KBR capability known as the Infinity Filter Framework (IFF) together with NASA's General Mission Analysis Tool[2] (GMAT). The IFF provides the computational construct to create the filters used in processing and tracking these cislunar objects. GMAT's force models are integrated into the IFF as the filter's state evolution function or propagator. Further details are provided in the following sections. Finally, the behavior of the estimation filters is analyzed when processing the different observation sets.

---

[1] The $\mathcal{L}1$ Halo family (i.e., H1) is truncated to include only the orbits that span the bifurcation points between the $\mathcal{L}1$ Lyapunov family (i.e., L1) and the W4W5 axial family.

[2] https://code.nasa.gov/?q=gmat

2. ORBITS AND OBSERVATIONS

In general, periodic orbits are special types of solutions of a dynamical system of the form,

$$\frac{dX}{dt} = f(X, t) \tag{1}$$

that satisfy the definition,

$$X(t) = X(t + T), \ \forall \, t \in R^1 \tag{2}$$

These periodic orbits are "closed" or "repeat" generally only in the synodic frame. Details for the resulting 31 families of orbits can be found in our previous year's AMOS conference paper [1]. In this paper, we explore three CR3BP elemental periodic orbit families: the planar L1 (long-period Lyapunov) family emanating from the $\mathcal{L}1$ Lagrange point, the H1 (halo) family which bifurcates from the L1 family at the L11 branch point, and the W4W5 (continuous east-west axial) family connecting from $\mathcal{L}4$ and $\mathcal{L}5$ Lagrange points and intersecting the H1 family at the H11 branch points. Note that for the H1 family, the nominal manifold is divided into northern and southern halves for those orbits near the Moon; here, only the northern sub-family is used. From these families, we down-select further to focus on fifteen individual orbits, each of which is differentially corrected to find the nearest[3] "periodic" orbit in the full-ephemeris model (salient features shown in Table 1). Figure 1 shows the fifteen use cases: (left) the seed CR3BP orbits and (right) the differentially corrected orbits in an Earth-Moon pulsating synodic frame. The non-repeating behavior of the differentially corrected orbits is primarily due to the ellipticity of the Moon's orbit.
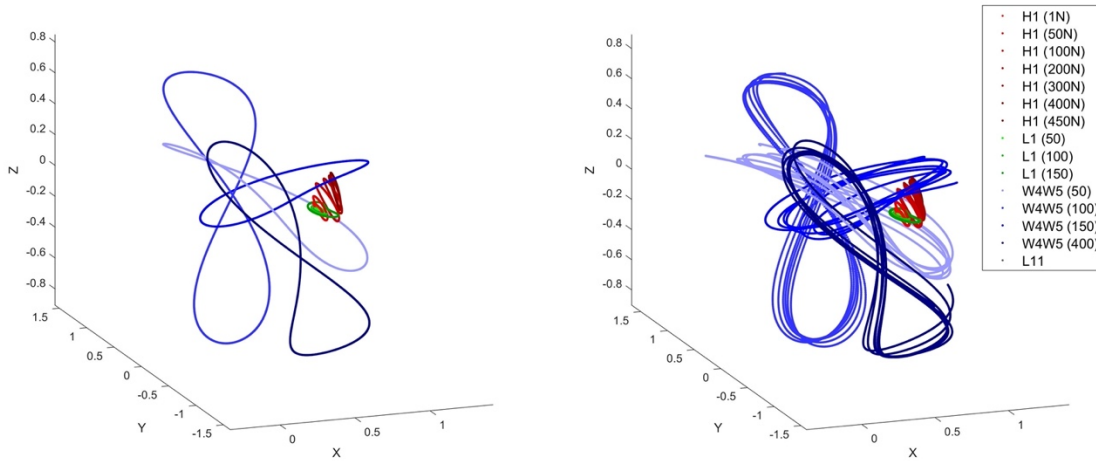

Figure 1. Use case orbits: (left) CR3BP seed solutions in the synodic frame and (right) differentially corrected trajectories, scaled to instantaneous Moon distances, in a pulsating synodic frame.

Table 1. Salient features of individual, differentially corrected, cislunar "periodic" orbits.

Identifier	Jacobi Energy	Synodic period (days)	Days simulated
H1 (1N)	3.1743	11.927	69.2
H1 (50N)	3.1523	11.985	69.3
H1 (100N)	3.1168	12.093	69.4
H1 (200N)	3.0153	11.426	68.1
H1 (300N)	3.0003	8.740	52.3
H1 (400N)	3.0022	7.844	47.1

---

[3] Up to the accuracy of a user's force model configurations and convergence tolerances.

H1 (450N)	2.9910	8.068	48.5
L1 (50)	3.1793	11.846	69.1
L11 (~L1 (65) & ~H1 (1N))	3.1744	11.927	69.2
L1 (100)	3.1413	12.548	75.1
L1 (150)	3.0670	14.737	88.61
W4W5 (50)	2.7030	23.036	156.8
W4W5 (100)	1.9490	27.377	164.5
W4W5 (150)	2.7898	27.770	147.7
W4W5 (400)	2.1480	27.303	156.6

The same longitudinally separated notional Earth ground-based sensor sites as in the previous paper are used to ensure the object is continuously visible from at least one of the sites: Maui (20.7º N, 156.4º W), Azores (37.8º N, 25.5º W), and Cocos Islands (12.2º S, 96.9º E). Similar to the previous study, the forward light-curve modeling software Forge was used to generate the light curves. Forge is a KBR product written in MATLAB with the underlying structure using facet-based models. Observations with 1 arcsecond astrometric uncertainty were created at a cadence of 600 seconds for a diffuse sphere (1 m^2 cross sectional area and 0.2 reflectance) and thresholds of object elevation > 10 degrees, Sun elevation < -10 degrees (Sun exclusion), object > 1 degree from limb of Moon (Moon exclusion), and object magnitude < 24. One arcsecond corresponds to about 1.86 km at the Moon's distance. Duplicate times (e.g., two sensors observing an object simultaneously) are removed. Figure 2 shows the 10,720 simulated observations for the H1 (100N) orbit case. Clearly evident are periods near the new moon when not only the object becomes dimmer as it becomes more backlit, but the object has fewer observations at each sensor site per night and there is a period of time when the object is not observed at all. Different cadence rates and/or data gaps are obtained by subsampling the data sets as desired.
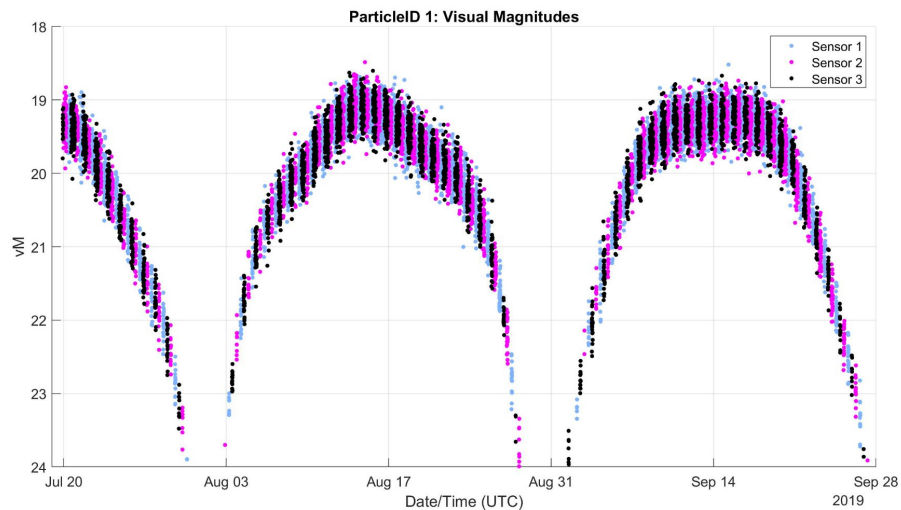

Figure 2. Light curve representing the Full set (all sensors, all observations), for the H1 (100N) cislunar object. Note that the periods with no observations correspond to lunar exclusion and poor lighting conditions due to the new Moon phase.

In addition to the full data set for each orbit (all three sensors at 600 seconds cadence), three subsets varying the number of sensors and their sensitivities are analyzed: (1) all three sensors at 1-hour cadence, (2) single sensor at 1-hour cadence, and (3) single sensor at 1-hour cadence and limiting magnitude set at 20 instead of 24. The process noise was set to 10^{-11} km/s^2 for each of the radial, in-track, and cross-track directions. Figure 3 shows the light curves for the full H1 (100N) data set of 10,720 simulated observations as compared to the three decimated subsets of 1787, 598, and 413 simulated observations, respectively. For convenience, the four data sets are herein labeled: Full set, Subset 1, Subset 2, and Subset 3.
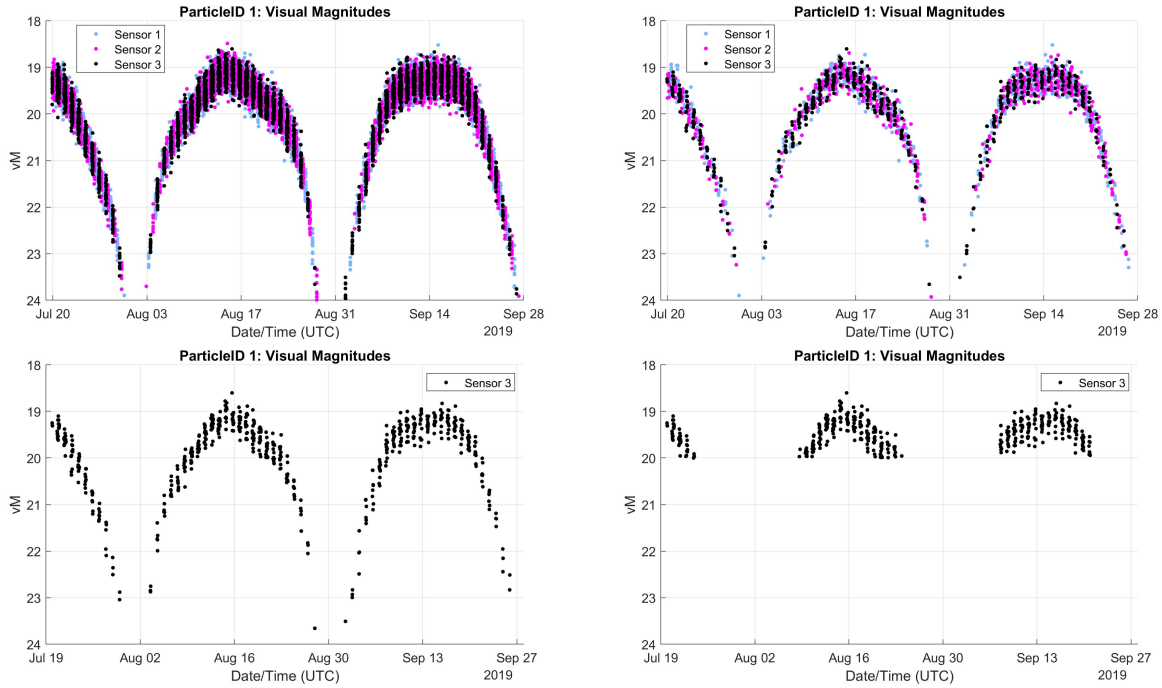
Figure 3. Applying the decimation strategy varying data cadence, data density, data quality, and data span creates the testable data sets for this work (only photometric observations shown here): light curves for Full set (upper left), Subset 1 (upper right), Subset 2 (lower left), and Subset 3 (lower right) for orbit H1 (100N).

3. ESTIMATION ENGINE

In order to process the synthetic observations generated in the previous section, we employ a unique filtering concept to assemble an advanced estimation engine from modular components: the Infinity Filter Framework (IFF).
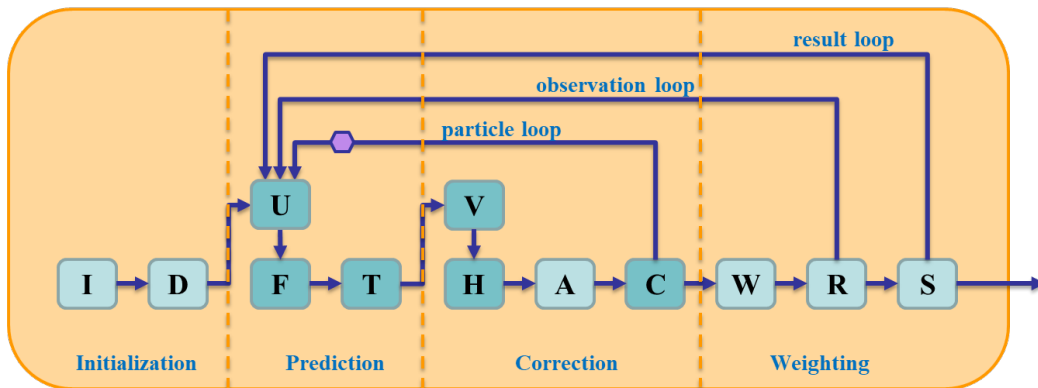

Figure 4. IFF module schematic. On color shading: darker = parallel, lighter = serial.

The IFF is a KBR, MATLAB-based, software suite that encodes a generalized framework capable of constructing various types of filters from key components or modules. The framework's modular design provides an unbounded upper limit on the number of possible combinations or varieties of modeling approaches, giving the developer or analyst an open design and implementation space in which to achieve their objectives. Its particle-like flavor is derived from agent-based modeling principles, allowing for the developer or analyst to create uniquely customizable particles for each agent within their particular population modeling schema. This strategy is a key departure from the

current space domain awareness (SDA) filtering paradigm, as the IFF facilitates adaptive state estimation and parameter inference, while allowing high levels of customization, learning, and optimization at the agent level. Figure 4 outlines the IFF's structure with regards to the various modules employed and Table 2 details each module and its function.

Table 2. IFF module descriptions.

Module	Description
I	**Initialization** – unique to each use case and used to set up parameters and state
D	**Data** – loads initial state and covariance as well as observations to be used by filter
U, V	**Sigma Points** – generates sigma points; Module-U is propagated by the state function and/or Module-V is used by the measurement function. In the degenerate case, these two modules are identical.
F	**State Function** – the dynamics model for the particular use case. For orbital dynamics, this function is the orbit propagator (e.g., GMAT R2020a)
T	**Time Update** – the time update in the estimation filter
H	**Measurement Function** – the observation-state mapping model
A	**Association** – used to associate an observation to a particular model
C	**Measurement Update** – the measurement update in the estimation filter
W	**Weighting** – the weighting function used to evaluate the weight of each particle
R	**Resampling** – how new particles are formed from the old particles at each time step (optional)
S	**Smoothing** – implementation of backwards smoothing (optional)

A critical defining feature of any estimation engine is its encoding of the state function (Module-F). For our purposes, we choose NASA's GMAT software, a high-fidelity orbital dynamics package capable of modeling perturbed 3-body dynamics [5]. GMAT is self-described as "the world's only enterprise, multi-mission, open source software system for space mission design, optimization, and navigation ... supporting missions in flight regimes ranging from low Earth orbit to lunar, libration point, and deep space missions"[4]. Because of the modular nature of the IFF, only a simple wrapper function is required to fully integrate GMAT's propagator into the IFF.

4. ANALYSIS AND RESULTS

4.1 Baseline unscented Kalman filter

Before using multiple particles in the IFF to implement a Gaussian Mixture Model (GMM), a single particle was employed to establish a baseline performance for tracking cislunar objects. This particle encoded an unscented Kalman filter (UKF) with Gaussian uncertainty. Two separate use cases were addressed, one using 2-body dynamics and the other using 3-body dynamics (including the Moon's gravitational influence) in the state function.

Table 3 and Table 4 show the maximum and median measurement innovation after the first new moon during the observations (epoch 2019 Aug 01) using 2-body and 3-body dynamics, respectively, for the orbits listed in Table 1. Yellow highlights median values over 0.1 arcminutes (maximum values over 5 arcminutes). Similarly, red highlights median values over 1 arcminute (maximum values over 15 arcminutes). With the estimation filter using the 2-body dynamics (an obvious force model mismatch), it is not surprising that the object was lost after the first data gap in all of the cases (see numeric summary in Table 3). On the other hand, the estimation filter using 3-body dynamics was able to maintain tracking the object with relatively small uncertainties – a consequence that would allow for continuous tracking in most cases. As expected, increasing the data gap length and frequency (moving from denser to sparser subsets) increases the innovations in kind. This correlation, between data gap length and frequency versus

---

[4] https://software.nasa.gov/software/GSC-18094-1

innovations magnitude, is the most pronounced when processing Subset 3 (single sensor and limiting magnitude of 20, thus larger data gaps near the new moon). Also note how H1 (1N) and L11, although nearly identical orbits, yield surprisingly different results for Subset 3. This sensitivity to initial conditions highlights the chaoticity of the problem near a theoretical bifurcation point (see numeric summary in Table 4). There also exists unintuitive variations seemingly as a function of the orbit; the reasons for these behaviors are unclear at the moment.

Table 3. UKF using 2-body dynamics, root-mean-square measurement innovation (arcminutes).

Orbit	Full set max error	Full set med error	Subset 1 max error	Subset 1 med error	Subset 2 max error	Subset 2 med error	Subset 3 max error	Subset 3 med error
H1 (1N)	2269.31	60.03	1281.67	85.99	2117.61	75.47	10183.21	781.53
H1 (50N)	1700.97	110.22	1622.30	128.41	2458.02	130.67	7614.04	581.39
H1 (100N)	2186.54	168.27	2330.90	189.95	2592.24	199.50	6307.67	252.87
H1 (200N)	3140.79	255.61	3182.11	301.41	3343.16	291.34	8819.51	670.35
H1 (300N)	2958.80	275.11	2824.73	301.33	3758.72	343.33	9086.98	246.25
H1 (400N)	2429.72	275.76	2233.52	304.64	2039.04	308.81	7182.55	116.01
H1 (450N)	2156.69	275.45	1980.22	305.74	2151.30	262.06	4131.48	160.65
L1 (50)	1925.66	48.06	1228.05	75.10	1683.32	69.99	5948.76	267.34
L11	2231.28	59.35	1263.43	85.66	2034.97	78.41	10888.98	802.64
L1 (100)	2181.77	107.79	2523.89	144.75	2161.08	128.00	8798,18	500.47
L1 (150)	4325.10	153.20	3851.42	293.62	4099.26	255.75	8768.41	855.76
W4W5 (50)	630.69	35.08	693.43	68.97	2612.01	56.82	10141.09	167.70
W4W5 (100)	23.72	3.54	31.35	7.04	95.35	5.10	422.02	8.25
W4W5 (150)	2034.57	25.51	2130.53	54.33	2127.66	70.15	10969.05	576.20
W4W5 (400)	35.23	2.87	46.42	4.79	102.97	6.43	8761.80	263.73

Table 4. UKF using 3-body dynamics, root-mean-square measurement innovation (arcminutes).

Orbit	Full set max error	Full set med error	Subset 1 max error	Subset 1 med error	Subset 2 max error	Subset 2 med error	Subset 3 max error	Subset 3 med error
H1 (1N)	0.09	0.020	0.44	0.020	1.05	0.021	7625.03	620.93
H1 (50N)	0.13	0.020	0.42	0.020	0.29	0.020	163.03	0.022
H1 (100N)	0.22	0.020	0.23	0.020	0.16	0.021	84.53	0.022
H1 (200N)	0.33	0.021	0.30	0.021	0.18	0.022	15.59	0.021
H1 (300N)	0.08	0.021	0.12	0.020	0.25	0.022	1.48	0.022
H1 (400N)	0.20	0.021	0.15	0.022	0.07	0.023	14.01	0.026
H1 (450N)	0.09	0.020	0.28	0.022	0.10	0.021	2.10	0.023
L1 (50)	0.12	0.020	0.16	0.020	0.57	0.020	377.62	0.188
L11	0.10	0.020	0.09	0.021	0.47	0.021	390.98	0.954
L1 (100)	0.48	0.020	0.13	0.020	0.84	0.021	3121.50	9.510
L1 (150)	0.26	0.020	0.34	0.021	0.41	0.021	33.34	0.021
W4W5 (50)	0.07	0.020	0.07	0.020	0.07	0.019	0.25	0.021
W4W5 (100)	0.07	0.020	0.07	0.020	0.14	0.021	0.29	0.020
W4W5 (150)	0.08	0.020	0.06	0.020	0.06	0.021	0.21	0.020
W4W5 (400)	0.08	0.020	0.07	0.020	0.06	0.021	0.46	0.022

Absolute performance is measured by comparing the estimated state to the truth state. Figure 5 graphically shows the combined measurement innovation and the 1-σ uncertainty of the right ascension and declination observations for the H1 (100N) orbit using 3-body dynamics. Figure 6 graphically shows the position magnitude error from the truth and 3-σ uncertainty for the H1 (100N) orbit using 3-body dynamics, while also conveys the variability in convergence depending on the data density and object observability. Uncertainty growth is proportionate to data gap length and the nonlinearity of the local dynamics.
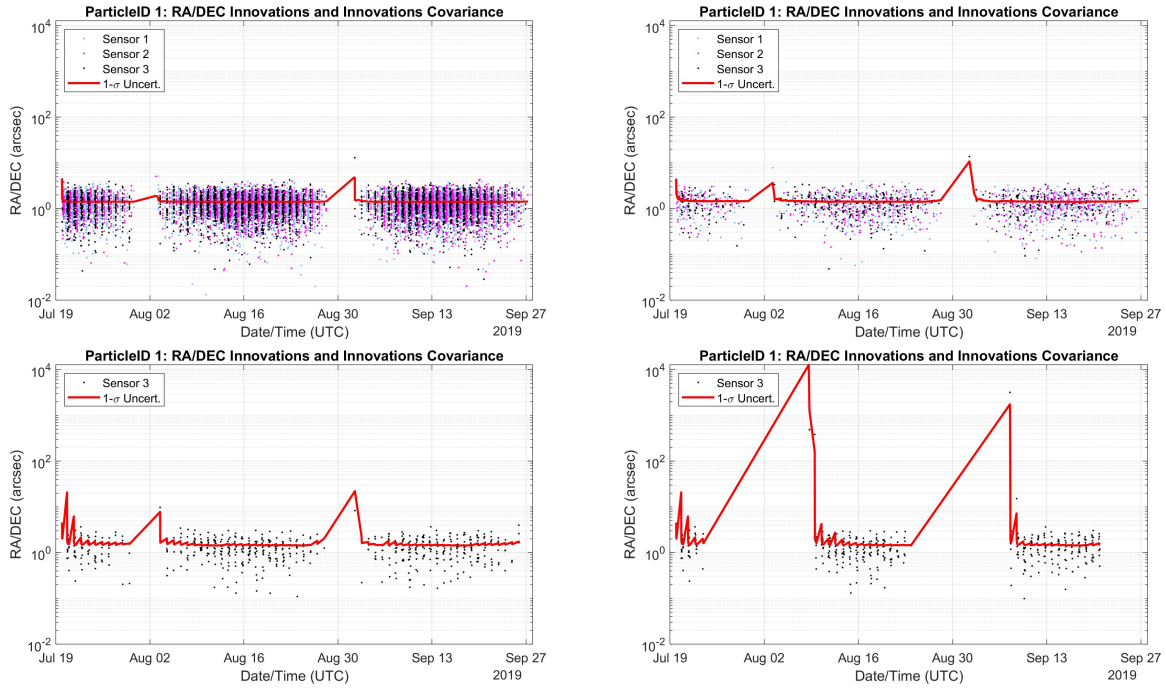
Figure 5. Measurement innovation and uncertainty of UKF with 3-body dynamics for Full set (upper left), Subset 1 (upper right), Subset 2 (lower left), and Subset 3 (lower right) for orbit H1 (100N), showing increasing innovation and uncertainty as the amount of data decreases and length of data gaps increase (going from Full set to Subset 3). Note that all cases reach the 1 arcsecond RA/DEC measurement error floor when data is available.
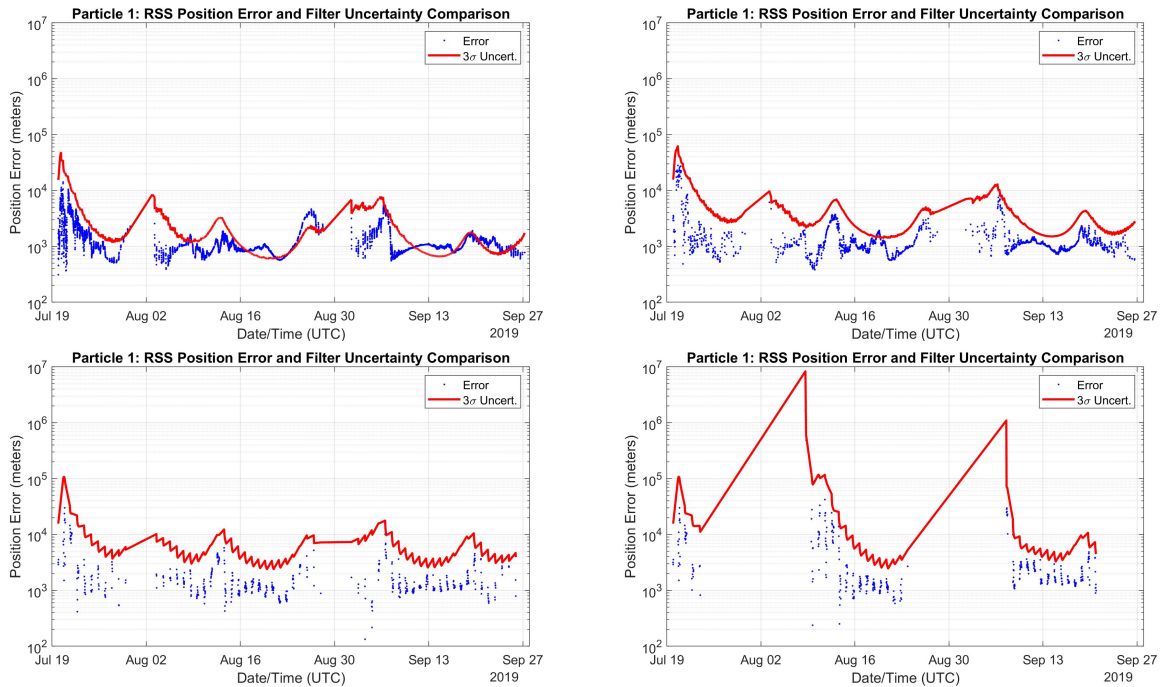

Figure 6. Position magnitude error and uncertainty of UKF with 3-body dynamics for Full set (upper left), Subset 1 (upper right), Subset 2 (lower left), and Subset 3 (lower right) for orbit H1 (100N), showing increasing error and uncertainty as the amount of data decreases and length of data gaps increase (going from Full set to Subset 3). Note that all cases maintain track of the object through data gaps.

Table 5 shows the maximum and median of the root-mean-square state positional errors after the first new moon and Table 6 shows the maximum and median state Mahalanobis distance after the first new moon. In Table 5, values over 100 km are highlighted in yellow while those over 1000 km are highlighted in red. Even from the limited use cases so far, it can be reasonably concluded that a single UKF using 3-body dynamics does a fairly good job at keeping track of an object in cislunar orbit and provides a good position estimate and uncertainty. There is a point, however, as can be seen with Subset 3, where large gaps in the data prevent the UKF from adequately tracking the object (most pronounced near the L11 branch point for the H1 (1N), L1 (50), L11, and L1 (100) orbits). The W4W5 orbits selected for this study, which stay far removed from the vicinity of the Moon for their entire orbits, perform particularly well even with the limited observations in Subset 3. This behavior is still true for W4W5 (100) and W4W5 (400), which are relatively close to the V41 and V51 branch points in the V4V5 family respectively (W4W5 (108) and W4W5 (402) would be closest). In Table 6 values over 10 are highlighted in yellow while those over 100 are highlighted in red.

Table 5. UKF using 3-body dynamics, root-mean-square position state error (km).

Orbit	Full set max error	Full set med error	Subset 1 max error	Subset 1 med error	Subset 2 max error	Subset 2 med error	Subset 3 max error	Subset 3 med error
H1 (1N)	4.74	0.77	6.76	0.90	8.56	1.36	2455962	895339.91
H1 (50N)	4.46	0.90	7.23	1.18	8.75	1.25	3942.63	1.75
H1 (100N)	8.07	0.97	8.54	1.07	10.14	1.84	1638.58	1.64
H1 (200N)	12.80	1.75	7.02	1.63	7.16	1.85	15.23	2.23
H1 (300N)	5.86	1.80	4.04	2.03	5.27	2.33	10.05	3.66
H1 (400N)	3.16	1.40	4.99	1.21	6.31	1.56	504.09	2.20
H1 (450N)	3.17	1.36	3.31	1.48	5.55	1.59	117.58	2.58
L1 (50)	3.58	0.80	8.30	0.92	11.95	1.51	16963.59	202.70
L11	5.01	0.37	8.26	0.69	11.70	1.07	314247.41	1983.51
L1 (100)	24.89	1.18	13.21	1.28	12.86	1.58	1234161	40094.29
L1 (150)	18.22	3.47	24.46	3.48	23.02	3.65	16.98	3.88
W4W5 (50)	5.57	0.20	7.42	0.40	5.53	0.97	11.52	0.98
W4W5 (100)	3.15	0.49	3.37	0.70	5.29	0.97	14.60	2.88
W4W5 (150)	3.73	0.21	4.05	0.37	4.38	0.76	11.63	1.09
W4W5 (400)	1.32	0.22	1.65	0.41	5.55	0.94	17.72	1.55

Table 6. UKF using 3-body dynamics, position state Mahalanobis distance.

Orbit	Full set max error	Full set med error	Subset 1 max error	Subset 1 med error	Subset 2 max error	Subset 2 med error	Subset 3 max error	Subset 3 med error
H1 (1N)	8.89	5.13	5.02	2.40	3.58	1.56	469899.60	307448.09
H1 (50N)	18.00	9.30	8.89	4.83	4.28	2.41	7.41	2.53
H1 (100N)	22.45	13.29	11.12	6.34	5.30	2.88	7.68	2.87
H1 (200N)	18.31	11.37	7.81	4.73	6.18	2.89	6.51	2.80
H1 (300N)	19.89	9.96	7.82	4.68	5.09	2.53	5.09	3.50
H1 (400N)	18.59	9.14	8.29	3.64	4.90	2.75	4.94	2.30
H1 (450N)	17.82	9.18	7.56	4.55	4.64	2.15	3.79	2.94
L1 (50)	8.20	4.83	5.67	2.41	3.91	1.85	332.99	31.81
L11	3.64	1.63	3.19	1.32	3.10	1.08	39455.59	582.05
L1 (100)	16.45	8.82	9.16	4.39	5.12	2.14	120092	7986.40
L1 (150)	16.50	12.64	8.51	5.72	5.43	3.49	5.07	2.57
W4W5 (50)	3.29	1.30	3.61	1.17	3.56	1.32	3.88	1.50
W4W5 (100)	8.40	2.37	5.20	2.08	3.71	1.64	4.96	2.37
W4W5 (150)	3.61	1.50	2.85	1.34	3.36	1.16	2.66	1.21
W4W5 (400)	3.82	1.47	3.24	1.30	3.52	1.23	3.86	1.12

4.2 Gaussian Mixture Model

Multiple particles within the IFF can be employed to represent different components in a Gaussian Mixture Model (GMM). Implementing the GMM requires adjustments to Module-W to compute the weighting of the different components of the GMM and to Module-R to trigger during a split or a collapse, from a single Gaussian to a GMM or from a GMM to a single Gaussian, respectively. For simplicity in this work, the number of Gaussian components is set to either three or five. As a first choice, we choose to split the single Gaussian at the time step before the first data gap using component splitting libraries [4], for both our three- and five-component cases. In terms of how the splitting is decided, the general strategy is to split along the direction of the largest eigenvalue of the state covariance matrix.

For illustrative purposes, a point-solution comparison is presented to showcase the difference between using a single-Gaussian UKF and a five-component GMM within the cislunar domain to build understanding around the impacts of nonlinearities on uncertainty realism. The a-priori uncertainty is normally distributed with a 10-km position and 1-m/s velocity RSS. Monte Carlo particle "shadows" or orthogonal projections are shown in gray to provide context. We use the geocentric celestial reference frame (GCRF) with a rectangular coordinate system oriented and centered on the radial, in-track, and cross-track (RIC) axes of the mean particle at epoch.

The comparative figures (Figure 7 and Figure 8) focus exclusively on velocity because the uncertainty deformations are more pronounced and are thus easier to intuit. The red points are the 2N+1 sigma points; (left) for a single UKF and (right) for each GMM component as distinguished by different markers/symbols. The green contours on the orthogonal planes are the bivariate marginal PDF contours for mean/covariance derived from the sigma points to provide overlapping comparisons against the gray shadows of the Monte Carlo run. As expected, the two PDF representations are almost identical at the starting time. Note, in Figure 7, the component splitting occurs along the radial velocity direction (here, corresponding to the axis containing the most uncertainty growth).
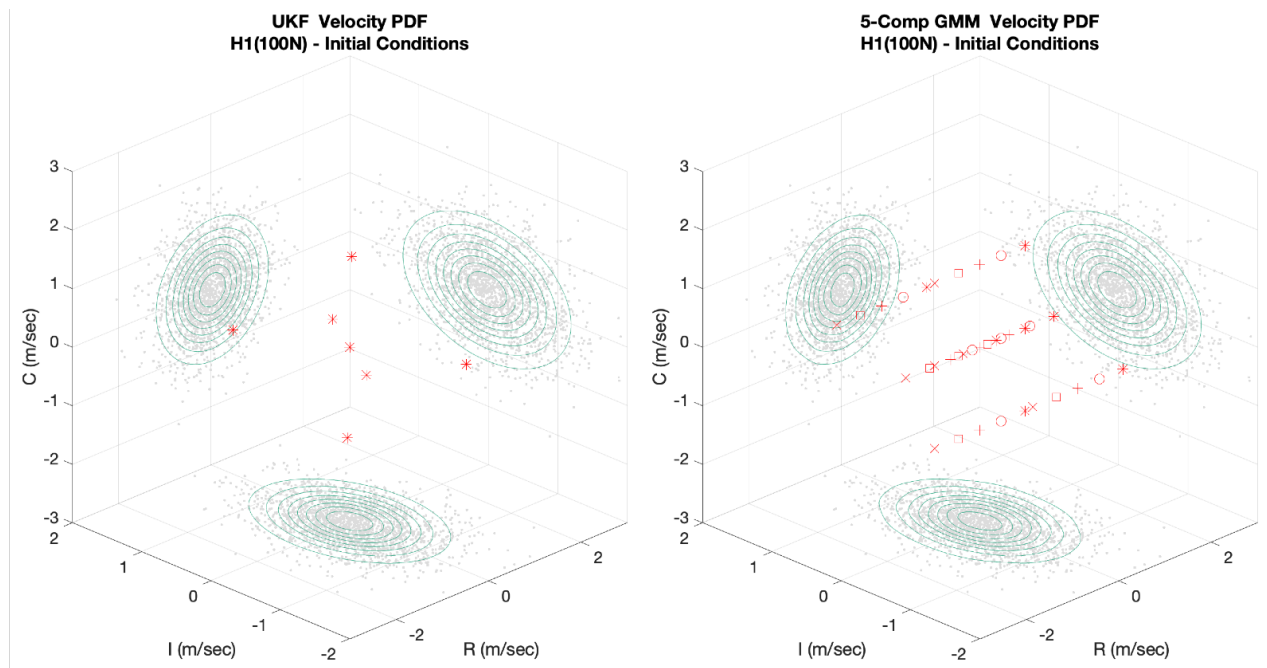

Figure 7. UKF (left) and 5-comp. GMM (right) velocity sigma point initial conditions for orbit H1 (100N); different marker types distinguish the different components of the GMM. Note the spread in the sigma points achieved by the multiple components is exclusively in the radial velocity direction.

Figure 8 plots the Monte Carlo, UKF, and five-component GMM after propagating for about seven days. The GMM better represents the Monte Carlo behavior (shadowed points) compared to a single Gaussian, highlighted by the marginal PDF contours. While the goodness of the fit and the relative difference between the two methods depends

on many factors, the overall sentiment is that a GMM representation of uncertainty is superior at modeling nonlinear growth (e.g., quantified by a likelihood agreement [4]).
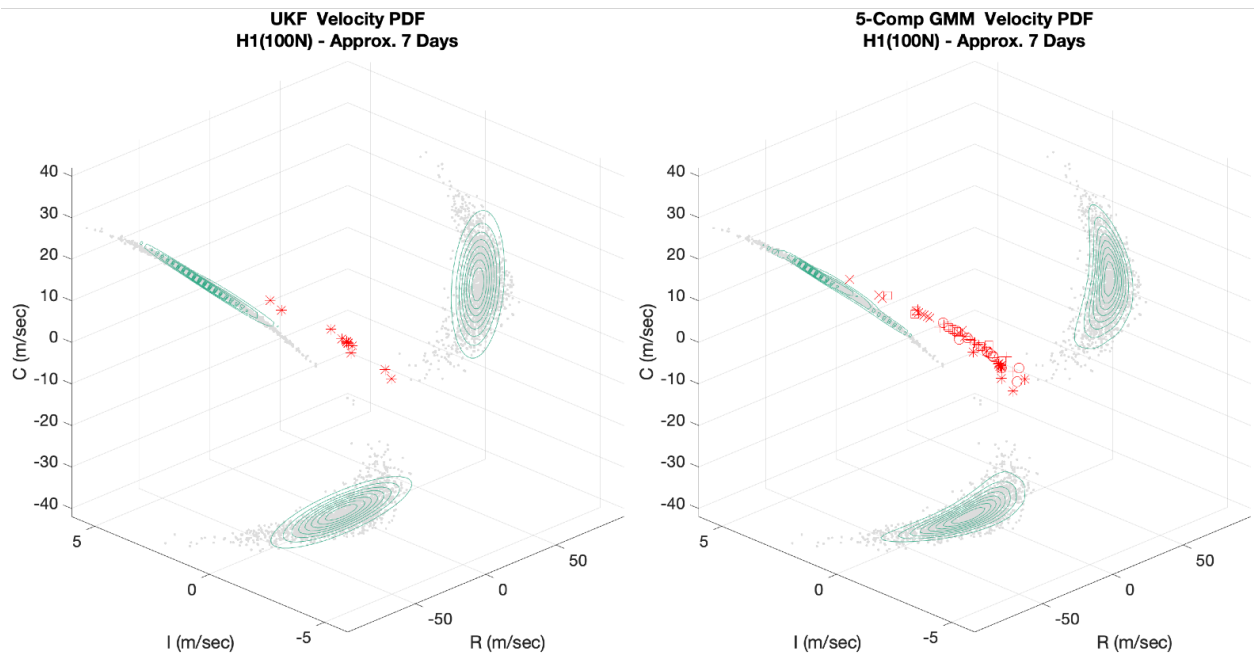

Figure 8. Approximate 7-day propagation for 2000-point Monte Carlo simulation; comparing UKF (left) and 5-comp. GMM (right) velocity marginal PDFs for orbit H1(100N). The curvature in the GMM contours clearly achieves a better fit with the Monte Carlo samples than the UKF covariance.

To see how the GMM's improved uncertainty modeling affects tracking performance, we conducted a study using 3-body dynamics in each of the estimation engines including a one-component GMM (i.e., a UKF), three-component GMM, and five-component GMM, while processing Subset 3 (the data set with the largest time gaps where the UKF faltered).

Table 7 and Table 8 summarily list the pertinent performance values together (the first two columns, pertaining to the UKF runs, are identical to the last two columns listed in Table 4 and Table 5 respectively). As in Table 4, Table 7's maximum/median values greater than 5/0.1 arcminutes are highlighted in yellow while those greater than 15/1 arcminutes are highlighted in red. As in Table 5, Table 8's values greater than 100 km are highlighted in yellow while those greater than 1000 km are highlighted in red.
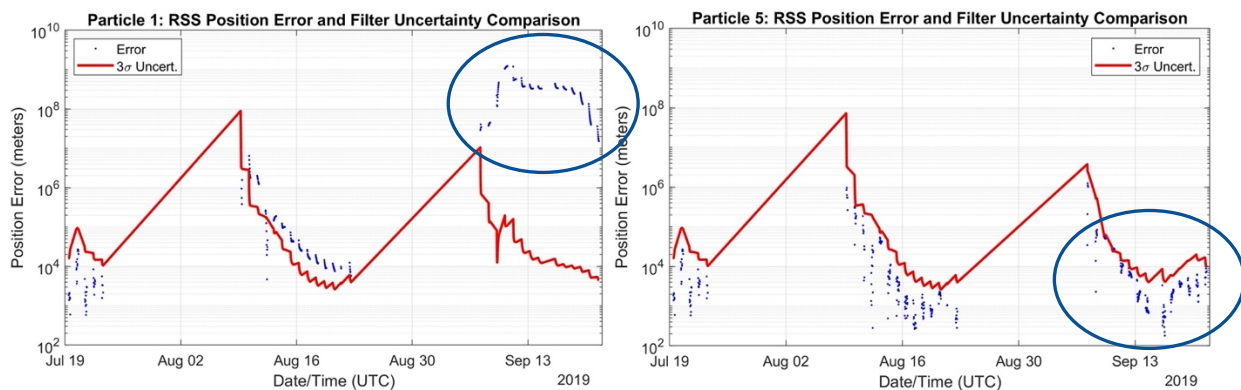

Figure 9. Position magnitude error and uncertainty for Subset 3 for orbit L1 (100), highlighting (left) the UKF losing track of the object after the second large data gap and (right) the 5-component GMM maintaining track throughout.

Both performance measures improve when using a GMM over the single-component UKF (most noticeably in H1 (1N) and L1 (100)). Of significant note, where the UKF failed to adequately track the object in the H1 (1N), L1 (50) and L1 (100) cases, the L1 (100) orbit did converge with the three-component GMM, and all converged with the five-component GMM. Figure 9 contrasts the UKF losing track of the cislunar object after the second large data gap with the five-component GMM configuration maintaining track throughout. Strangely, the L11 branch point orbit, despite being nearly identical to the H1 (1N) orbit, failed to converge with all filters; while the precise reason is unclear, the prevailing explanation points to the high degree of nonlinearity of the problem.

In summary, of the fifteen orbits analyzed, one failed to converge in all instances (L11); three failed to converge with the UKF, but did converge with the GMMs (H1 (1N), L1 (50), and L1 (100)); three improved in one or more measure from the UKF to GMMs (H1 (100N), H1 (200N), L1 (150)); and eight were about the same from the UKF to GMMs (H1 (50N), H1 (300N), H1 (400N), H1 (450N), W4W5 (50), W4W5 (100), W4W5 (150), W4W5 (400)).

Table 7. UKF versus GMM performance processing Subset 3, measurement innovation (arcminutes).

Orbit	UKF max error	UKF med error	three-comp GMM max error	three-comp GMM med error	five-comp GMM max error	five-comp GMM med error
H1 (1N)	7625.03	620.930	423.64	1.077	134.87	0.022
H1 (50N)	163.95	0.022	211.46	0.022	179.34	0.022
H1 (100N)	84.53	0.022	100.19	0.021	50.82	0.021
H1 (200N)	15.59	0.021	7.12	0.022	3.66	0.021
H1 (300N)	1.48	0.022	0.93	0.022	0.76	0.022
H1 (400N)	14.02	0.026	13.73	0.026	13.60	0.026
H1 (450N)	2.10	0.023	2.10	0.023	2.10	0.023
L1 (50)	377.62	0.188	352.09	0.193	299.73	0.022
L11	390.62	0.954	420.11	0.783	444.28	0.882
L1 (100)	3121.50	9.510	105.72	0.024	44.43	0.022
L1 (150)	33.34	0.021	13.16	0.021	10.70	0.021
W4W5 (50)	0.25	0.021	0.25	0.021	0.25	0.021
W4W5 (100)	0.29	0.020	0.29	0.020	0.29	0.020
W4W5 (150)	0.21	0.020	0.14	0.020	0.11	0.020
W4W5 (400)	0.26	0.022	0.44	0.022	0.42	0.022

Table 8. UKF versus GMM performance processing Subset 3, root-mean-square position state error (km).

Orbit	UKF max error	UKF med error	three-comp GMM max error	three-comp GMM med error	five-comp GMM max error	five-comp GMM med error
H1 (1N)	2455962.49	895339.91	82518.46	8088.49	5077.12	3.06
H1 (50N)	3942.63	1.75	3196.12	1.68	2129.28	1.61
H1 (100N)	1638.58	1.64	567.70	1.61	237.31	1.38
H1 (200N)	15.23	2.23	15.77	2.21	17.22	2.14
H1 (300N)	10.05	3.66	10.05	3.65	10.05	3.64
H1 (400N)	504.09	2.20	499.92	2.17	498.74	2.18
H1 (450N)	117.58	2.58	117.41	2.58	117.33	2.58
L1 (50)	16963.59	202.70	14324.02	119.83	22115.63	5.93
L11	314247.41	1983.51	105569.42	2414.54	204529.78	6543.40
L1 (100)	1234160.97	40094.29	48932.98	4.91	15183.17	3.18
L1 (150)	16.98	3.88	16.62	3.85	16.71	3.71
W4W5 (50)	11.52	0.98	11.52	0.98	11.52	0.98
W4W5 (100)	14.60	2.88	14.61	2.88	14.61	2.88
W4W5 (150)	11.63	1.09	11.63	1.09	11.63	1.09
W4W5 (400)	17.72	1.55	17.72	1.55	17.72	1.55

5. SUMMARY AND FUTURE WORK

This paper summarizes preliminary efforts focused on tracking and estimation approaches for objects in cislunar orbits and aims to help build high-level intuitions on different aspects of the estimation problem for the cislunar domain. Unsurprisingly, the use of robust 3-body dynamics is essential in providing accurate predictions and maintaining custody of these objects. Filters using traditional 2-body dynamics are demonstrated to fail quickly after data gaps in every use case tested. The UKF provides relatively good results for a variety of orbits and data cadences, while the GMM demonstrates promise in improving performance through data gaps. The incredible levels of nonlinearity evident in the cislunar domain present stressing challenges for the estimation and custody of cislunar objects.

The compounding effects of low observability and orbit maintenance maneuvers must be addressed in future work, as these factors will definitely be present and will significantly increase the difficulty level in maintaining robust tracks on cislunar objects. Beyond elemental periodic orbits, cislunar space admits a wide variety of other trajectory structures (e.g., quasi-periodic tori, invariant manifolds, homo-/hetero-clinic connections, resonance orbits) that should be systematically analyzed. From the remote sensing perspective, further analysis is required to assess the filtering impacts from the variability of different sensor characteristics such as data type, noise, bias, and sensitivity. Varying the location of the sensors (to include space-based platforms) will be necessary for a more complete understanding of the art of the possible in terms of meeting mission goals. Finally, it is prudent to conduct a broader exploration of different filter constructs including process noise levels, the nature of the Gaussian splitting strategies, data association approaches, and others that may have significant influence on the resulting track quality.

6. REFERENCES

[1] Chow, C., Wetterer, C., Hill, K., Gilbert, C., Buehler, D., and J. Frith. Cislunar Periodic Orbit Families and Expected Observational Features. *The Advanced Maui Optical and Space Surveillance Technologies (AMOS) Conference*, Maui, HI, September 15-18, 2020.

[2] Doedel, E., Romanov, V., Paffenroth, R., Keller, H., Dichmann, D., Galan-Vioque, J., and A. Vanderbauwhede. Elemental Periodic Orbits Associated with the Libration Points in the Circular Restricted 3-Body Problem. *International Journal of Bifurcation and Chaos*, 17(8):2625-2677, 2007.

[3] Vutukuri, S. Spacecraft Trajectory Design Techniques Using Resonant Orbits. *M.S. Dissertation*, Purdue University, West Lafayette, IN, 2018.

[4] DeMars, K., Bishop, R., and M. Jah. A Splitting Gaussian Mixture Method for the Propagation of Uncertainty in Orbital Mechanics. *Advances in the Astronautical Sciences*, 140:1419-1438, 2011.

[5] Hughes, S., Qureshi, R., Cooley, S., and J. Parker. Verification and Validation of the General Mission Analysis Tool (GMAT). 10.2514/6.2014-4151, 2014.